

Health Monitoring of Li-ion Battery Systems: A Median Expectation Diagnosis Approach (MEDA)

Haris M. Khalid, *Member, IEEE*, Qadeer Ahmed, *Member, IEEE*, and Jimmy C.-H. Peng, *Member, IEEE*

Abstract—The operations of Li-ion Battery Management System (BMS) are highly dependent on installed sensors. Malfunctions in sensors could lead to a deterioration in battery performance. This paper proposed an effective health monitoring scheme using a median expectation-based diagnosis approach (MEDA). MEDA calculates the median of a possible set of values, rather than taking their weighted average as in the case of a standard expected mean operator. Furthermore, a smoother was developed to capture important patterns in the estimation. The resulting filter was first derived using a one-dimensional system example, where the iterative convergence of median-based proposed filter was proved. Performance evaluations were subsequently conducted by analyzing real-time measurements collected from Li-ion battery cells used in Hybrid Electric Vehicles (HEV) and Plug-in HEVs (PHEV) duty cycles. Results showed the proposed filter was more effective and less sensitive to small sample size and curves with outliers.

Index Terms—Battery diagnosis, Battery Management System (BMS), expected value, Kalman filter, lithium-ion batteries, mean, median.

ACRONYMS AND ABBREVIATIONS	
BMS	Battery Management System
MEDA	Median expectation-based diagnosis approach
HEV	Hybrid Electric Vehicle
PHEV	Parallel Hybrid Electric Vehicle
SoC	State-of-charge
TMS	Thermal Management System
VMS	Voltage Management System
SMS	Safety Management System
BCU	Battery Control Unit
ME-based KS	Median expectation-based Kalman smoother
MKF	Median Kalman filter
MKS	Median Kalman smoother
DT	Detection time
MDR	Missed Detection Rate
FDR	False Detection Rate
IT	Isolation time
MIR	Missed Isolation Rate
EKF	Extended Kalman filter
MSE	Mean Square Error
DST	Dynamic Stress rate

I. INTRODUCTION

LITHIUM-ION batteries are popular in HEV market due to their high energy density and low maintenance cost [1–4]. However, their high capacity and large serial-parallel numbers of automotive lithium-ion batteries raised issues such as safety, reliability, cost, and uniformity. Lithium-ion batteries must operate in a reliable and safe operational range to prevent a decrease in lifetime, capacity, and safety related problems [5, 6]. For example, an extremely low-voltage or over-discharged battery may result in the collapse of the lattice and reduction of the electrolyte. High temperature operation can also cause the battery electrolyte to decompose, and produce combustible gas,

This work was developed on the data generated from the Center of Automotive Research Laboratory, Ohio State University, USA. The experiments were support by US DOE CERC under the project no. 60029877.

H. M. Khalid and J. C.-H. Peng are with the Department of Electrical Engineering and Computer Science, Institute Center for Energy, Masdar Institute of Science and Technology (MIST), Abu Dhabi, UAE. E-mail: mkhalid, jpeng@masdar.ac.ae

Q. Ahmed is with the Center for Automotive Research, The Ohio State University (OSU), Columbus, OH, USA. E-mail: ahmed.358@osu.edu

which exothermically reacts with the oxygen generated from the decomposition of the positive electrode. This may result in fire and thermal runaway [7–9]. On the other hand, low temperature operations can cause the breakdown of the cathode, and result in short-circuit [5, 10, 11]. Meanwhile, the imprecise calculation of SoC can easily trigger the overcharge or over-discharge situation, which may result in poor HEV efficiency [12, 13].

To keep the Li-ion battery system safe from these known issues, BMS is required to continuously track the battery performance with the help of on-board sensors. A battery pack is generally composed of several modules consisting of cells connected in-series to provide the desired voltage and in parallel to satisfy the capacity requirements. BMS includes the following subsystems and functions: 1) a TMS to keep the battery at optimal average temperature while minimizing temperature differences among cells, 2) a VMS to reduce cell-to-cell imbalances in voltage and SoC, 3) a SMS to electrically disconnect the battery in case of adverse conditions, and 4) a BCU. BCU controls all three subsystems, estimates battery parameters, and provides diagnostic and prognostic functions. This is done using a set of current, voltage, and temperature sensors connected to the BCU. It can be observed that BMS operations are highly dependent on healthy sensors. Any fault in these sensors, which are often neglected, can result in fatal consequences [5]. Some works were proposed for component-level analysis of faults [14–18]. However, limited attentions were given to sensor fault diagnosis for lithium-ion battery system at the system-level. This may lead to a false assumption that measurements collected from sensors are always accurate within subsystems. Therefore, this paper focuses on diagnosing system-level faults. This could provide access to have traceability against the system requirements established at each component-level. It could also provide the dynamic aspects of component interactions, ensuring component-level compatibility with the main system.

The contribution of this paper is to enhance the reliability of lithium-ion batteries at system-level by improving the estimation and detection capabilities of instant nonlinear faults in the forms of spikes and outliers. This was accomplished by first extracting the correlation information of the estimates. Subsequently, fault detection and isolation were performed using a proposed fault diagnosis scheme. The proposed scheme is named as MEDA approach. It is based on the principles of Kalman filter, which is widely applied for monitoring and estimating applications [19–25]. However, estimators developed from classic Kalman filter take the weighted average between the noisy observations and the prior measurements. This minimizes the expected value of the sample to be estimated, but does not guarantee a better measure of the central tendency if the sample size is small or contain outliers. To overcome this limitation, a novel nonlinear filter was derived using the median

expected value. The proposed enhancement was incorporated into the estimation step and integrated with a fault diagnosis scheme to monitor lithium-ion battery system.

An overview of the proposed MEDA scheme is illustrated in Fig. 1. Compared with its Kalman predecessors of [16] and [17] used in the same field, the proposed scheme improved the estimation and detection accuracy under random fault fluctuations. This was done by computing modal parameters from the input of a variable battery system, which is the current. Subsequently, estimation of voltage and temperature outputs of the battery system was computed using a ME-based KS estimator using (25)–(28), where derivations of the equations will be shown in the following sections. At this stage, random faults were injected in both outputs. The proposed filter was applied to detect these faults, thereby doing a residual generation using (29)–(37). The residual is a measure used to quantify the existence of a fault. To make residual evaluation of the signal, a fault threshold selection was also formulated using a coherence function (38)–(42). Once an accurate threshold was selected, faults could be isolated using a recognition model from (43). The isolation signal was represented on a binary scale.

The paper is organized as follows: The problem was formulated in Section II. The implementation and evaluation of the scheme were discussed in Section III. Conclusions and future work were drawn in Section IV.

II. PROBLEM FORMULATION

A. Median Expectation-Based Kalman filter with Gaussian Distributions

The derivation of the median expectation-based Kalman filter model assumed the state x of the battery system at a time $t + 1$ evolved from its prior state at time t as:

$$x_{t+1} = F_t x_t + B_t u_t + G_t w_t, \quad t = 0, 1, \dots, T \quad (1)$$

where $x_0 \in \mathbf{R}^r$ is the initial condition of the state, and $F_t \in \mathbf{R}^{r \times r}$ is a model matrix of the state response. Note each state depends on its covariates. The variable B_t is the input transition matrix, u_t is the input vector, G_t is the noise transition matrix, and $w_t \in \mathbf{R}^r$ is the random process noise. Finally, t is the time instant, and T refers to the number of time instants. Let the battery system described in (1) to be observed at time-instant t as:

$$z_t = H_t x_t + \nu_t \quad (2)$$

where $z_t \in \mathbf{R}^p$ is the observation output of state, p is the number of simultaneous observations for estimation made at time instant t , $H_t \in \mathbf{R}^{p \times r}$ is the observation matrix, x_t is the state matrix, and $\nu_t \in \mathbf{R}^p$ is the observation noise. The relationship of (1) and (2) was based on the following assumption.

Assumption II.1: The noises w_t and ν_t are all initially uncorrelated zero-median white Gaussian such that $\mathbf{E}_{\mu_{1/2}}[w_t] = \mathbf{E}_{\mu_{1/2}}[\nu_t] = 0, \forall t$. Note $\mathbf{E}_{\mu_{1/2}}$ denotes the median expectation operator, where $\mathbf{E}_{\mu_{1/2}}[w_i \nu_j^T] = 0$. Meanwhile, $\mathbf{E}_{\mu_{1/2}}[w_i w_j^T] = R_t \delta_{ij}$ when considering the noise process to be a serially uncorrelated, zero-mean, constant, and finite variance process. The variable R_t represents the covariance matrix, and δ_{ij} is a Kronecker delta function used for shifting the integer variable after the presence or absence of noise. Similarly, $\mathbf{E}_{\mu_{1/2}}[\nu_i \nu_j^T] =$

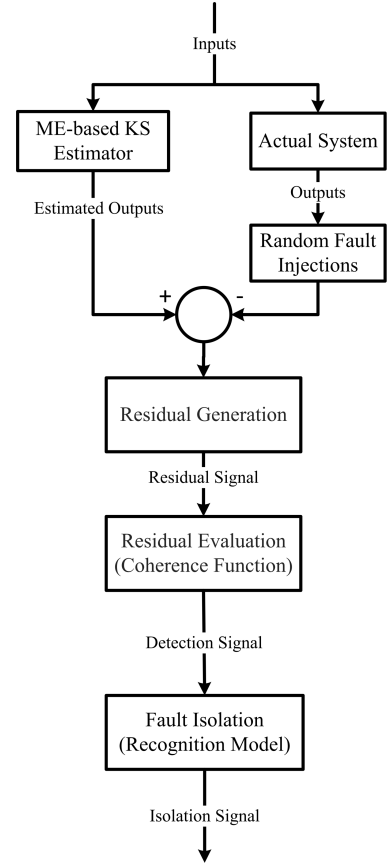


Fig. 1. Proposed MEDA based health monitoring scheme to detect and isolate sensor faults in Li-ion battery

$Q_t \delta_{ij}$ with Q_t being the process noise correlation factor. Based on the formulated system and observation models, the median-based Kalman filter could then be derived to enhance the estimation in the presence of outliers and small sample size. This required some additional properties of median expectation, which would be derived in the next subsection.

A.1 Properties of Median Expectation

The median-based expectation operator $\mathbf{E}_{\mu_{1/2}}$ was developed from the following definitions II.1, II.2 and II.4 as well as theorem II.1.

Definition II.1: Let X be a random variable. It admits a probability density function $f(x)$, where the standard expected value [26] is an infinite sum:

$$\mathbf{E}[X] = \sum_{-\infty}^{\infty} x f(x) \quad (3)$$

In the same manner, the median-based expected value of the random variable X is defined as:

$$P(X \leq \mu_{1/2}) = P(X \geq \mu_{1/2}) = \mathbf{E}_{\mu_{1/2}}[X] = \sum_{-\infty}^{\mu_{1/2}} x f(x) = \frac{1}{2} \quad (4)$$

The term $\mu_{1/2}$ is the calculated median for the random variable X . It is defined in a separable Hilbert space H over \mathbf{R}^d as:

$$\mu_{1/2} = \mathbf{E}_{\mu_{1/2}}(x_1, \dots, x_N) = \arg \min_{s \in H} \sum_{i=1}^N (\|X_i - s\|) \quad (5)$$

where $\|\cdot\|$ is its associated norm, and s is a real variable. When observing the sample values x_1, x_2, \dots, x_N , a median $\mu_{1/2}$ is

defined by the gradient equation from [27] as:

$$\mathbf{E}_{\mu_{1/2}}(X) = \sum_{i=1}^N \frac{X_i - \mu_{1/2}}{\|X_i - \mu_{1/2}\|} = 0 \quad (6)$$

The median $\mu_{1/2}$ always belongs to the convex hull of sample values x_1, x_2, \dots, x_N . It could be evaluated iteratively as:

$$\mu_{1/2,t+1} = \mu_{1/2,t} + \gamma_t \frac{X_{t+1} - \mu_{1/2,t}}{\|X_{t+1} - \mu_{1/2,t}\|} \quad (7)$$

Note the sequence of steps γ_t satisfies, $\gamma_t > 0$ for all time-instants $t \geq 1$. The properties to calculate (7) were outlined in theorem II.1.

Proof: This is shown in the Appendix. ■

Theorem II.1: Let X and Y be two random variables while c is a constant value. The following properties can be subsequently stated.

Property 1: If $c \in \mathbf{R}$, then $\mathbf{E}_{\mu_{1/2}}[cX] = c\mathbf{E}_{\mu_{1/2}}(X)$.

Proof: This is proved in the Appendix. ■

Property 2: If $a, b \in \mathbf{R}$:

$$\mathbf{E}_{\mu_{1/2}}[aX + bY] \simeq a\mathbf{E}_{\mu_{1/2}}X + b\mathbf{E}_{\mu_{1/2}}Y \quad (8)$$

Proof: This is proved in the Appendix. ■

Property 3: If X and Y are independent:

$$\mathbf{E}_{\mu_{1/2}}[XY] \approx \mathbf{E}_{\mu_{1/2}}(X)\mathbf{E}_{\mu_{1/2}}(Y) \quad (9)$$

Proof: It follows the proof of Property 2. ■

Property 4: If X is an independent variable, then for the higher moments of X , i.e. $\mathbf{E}_{\mu_{1/2}}[X^2]$,

$$\begin{aligned} \mathbf{E}_{\mu_{1/2}}[X^2] &= \mathbf{E}_{\mu_{1/2}}[(X - \mathbf{E}_{\mu_{1/2}}[X])^2] \\ &= \arg \min_{\theta_1} \{ |[X - \arg \min_{\theta_2} \{|X - \theta_2| \}]^2 - \theta_1 | \} \\ &= \arg \min_{\theta_1} \{ |X^2 - 2X(\arg \min_{\theta_2} |X - \theta_2|) \\ &\quad + (\arg \min_{\theta_2} |X - \theta_2|)^2 - \theta_1 | \} \end{aligned} \quad (10)$$

where θ_1 and θ_2 represents the expectation $\mathbf{E}_{\mu_{1/2,1}}$ and $\mathbf{E}_{\mu_{1/2,2}}$ respectively.

Definition II.2: According to [28], if the distribution has a finite variance, then the distance between the mean and the variance is bounded by one standard deviation:

$$|\mu - \mu_{1/2}| \leq \sigma \quad (11)$$

where σ is the standard deviation. Using the property of equality gives:

$$\begin{aligned} \mu_{1/2} - \mu &\leq \sigma \\ \mu_{1/2} - \mu - \sigma &\leq 0 \\ \mu_{1/2} - \mu - \sigma + f(\mu_{1/2}) &= 0 \\ \mu_{1/2} &= \mu + \sigma - f(\mu_{1/2}) \end{aligned} \quad (12)$$

where $f(\mu_{1/2})$ is calculated using definition II.3.

Definition II.3: $f(\mu_{1/2})$ could be computed according to the procedure illustrated in Fig. 2. To find the median function in the first iteration, a minimum of three sample data points are required. The standard deviation of this data set as well as the ramp robustness calculation for data points with an increasing order could be determined. From these values, the distance between the median and the mean could be computed. Similarly, the distance between the present data sample and the median could be found using a Chebychev window. Such approach

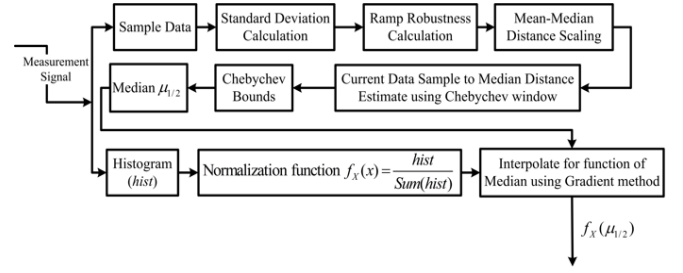


Fig. 2. Overview of the median function calculation

minimizes the Chebyshev norm of side-lobes for a given main lobe width for which the distance needs to be calculated. The computed distance gives the median of state x . In parallel, the histogram of the data sample from the state x is calculated as shown in Fig. 2. A normalization function is applied to adjust the values according to the sum of data samples. The normalization function and the median calculated from the Chebychev bounds are then used to interpolate for function of median. This could be achieved by the gradient method outlined by the following definition.

Definition II.4: Referring to [29], the distribution of the sample median from a sample size with a density function $f(\mu_{1/2})$ is asymptotically normal with a mean μ , and a variance σ^2 :

$$\frac{1}{4nf(\mu_{1/2})^2} \quad (13)$$

Note n is the sample size. Hence, the normal distribution could be defined as $f(x, \mu, \sigma) = \frac{1}{\sqrt{2\pi\sigma^2}} e^{-\frac{(x-\mu)^2}{2\sigma^2}}$. Using the definition of [29], let the sample to be of the size $m = 2n + 1$. The median-based normal distribution could then be expressed as:

$$f(x, \mu_{1/2}, \sigma) = \frac{1}{\sqrt{2\pi\sigma^2}} e^{-8f(\mu_{1/2})^2 m(x-\mu_{1/2})^2} \quad (14)$$

1) *Formulation of ME-Based KS based on Median Operator and First Principles*

Once the definitions and theorem were derived, a system model for Kalman filter using the median-based expectation operator was formulated. Suppose the estimated state at time-instant t for the time-sequence T is $\hat{x}_{t|t}$. Given the information of (2) and time sequence $T - 1$, the state prediction can be defined linearly with a conditional probability as:

$$\begin{aligned} \hat{x}_{t|t-1} &= \mathbf{E}_{\mu_{1/2}}[x_t | Z^{T-1}] \\ &= F_t \arg \min_x [x_{t-1} - \mu_{1/2,t-1}] + B_t u_t \end{aligned} \quad (15)$$

Note the process noise is assumed to have a zero median. Taking the difference between (1) and (15) gives:

$$\begin{aligned} x_t - \hat{x}_{t|t-1} &= F_t x_{t-1} + B_t u_t + G_t w_t - F_t \arg \min_x [x_{t-1} - \\ &\quad \mu_{1/2,t-1}] - B_t u_t \end{aligned} \quad (16)$$

Here $x_t - \hat{x}_{t|t-1}$ is equal to the covariance matrix matrix $P_{t|t-1}$ as followed by standard KF.

$$\begin{aligned} P_{t|t-1} &= F_t(x_{t-1} - \arg \min_x [x_{t-1} - \mu_{1/2,t-1}]) + G_t w_t \\ &= \mathbf{E}_{\mu_{1/2}}[F_t(x_{t-1} - \arg \min_x [x_{t-1} - \mu_{1/2,t-1}]) \\ &\quad + G_t w_t)(F_t(x_{t-1} - \arg \min_x [x_{t-1} - \mu_{1/2,t-1}]) \\ &\quad + G_t w_t)^T] \\ &= F_t \mathbf{E}_{\mu_{1/2}}[(x_{t-1} - \arg \min_x [x_{t-1} - \mu_{1/2,t-1}])(x_{t-1} \end{aligned}$$

$$\begin{aligned}
& - \arg \min_x [x_{t-1} - \mu_{1/2,t-1}]^T F_t^T + F_t \mathbf{E}_{\mu_{1/2}} [(x_{t-1} \\
& - \arg \min_x [x_{t-1} - \mu_{1/2,t-1}]) G_t w_t^T] + \mathbf{E}_{\mu_{1/2}} [G_t w_t \\
& (x_{t-1} - \arg \min_x [x_{t-1} - \mu_{1/2,t-1}])^T] F_t^T \\
& + G_t \mathbf{E}_{\mu_{1/2}} [w_t w_t^T] G_t^T \\
& = F_t P_{\mu_{1/2,t-1}|t-1} F_t^T + G_t Q_t G_t^T \quad (17)
\end{aligned}$$

The measurement updated equations for the estimated state \hat{x}_t and the covariance matrix P_t were derived from first principles based on (15) to (17). It followed the concepts outlined in [30]. Here, the estimation was determined using a probability density function (pdf) with normal distributions. A simple one-dimension system example based on vehicular motion was used to formulate the calculations of information gathered from the pdfs.

Assume an electric vehicle is constantly tracking to see if it is following a straight line. At each time instant, it seeks to know the position of the vehicle. This could be achieved by knowing the last known position of the vehicle and measurements gathered as the vehicle starts its motion at time-instant t_0 while following the whole time-sequence t_0^T . At a new time-instant, e.g. t_1 , the new position of the vehicle could be calculated by knowing the limitation such as velocity, acceleration, and deceleration. Now, suppose a position of the vehicle could be modeled by a Gaussian pdf with a known median and variance. When the vehicle moves, each new position is represented by a different Gaussian pdf. Similarly, the new position could again be estimated by the prediction from the last known position and the measurements of past observations. This is equivalent to multiplying two Gaussian pdfs assumed at different time-instants.

To consider multiplication of pdfs, let the median-based Gaussian distribution function for the prediction from the last known position to be:

$$f_1(x, \mu_{1/2,1}, \sigma) = \frac{1}{\sqrt{2\pi\sigma^2}} e^{-8f(\mu_{1/2,1})^2 m(x - \mu_{1/2,1})^2} \quad (18)$$

Next the median-based pdf for measurement could be assumed as:

$$f_2(x, \mu_{1/2,2}, \sigma) = \frac{1}{\sqrt{2\pi\sigma^2}} e^{-8f(\mu_{1/2,2})^2 m(x - \mu_{1/2,2})^2} \quad (19)$$

The best estimate could then be calculated by multiplying the information from the prediction (18), and the measurement of (19) such that:

$$\begin{aligned}
& [f_1(x, \mu_{1/2,1}, \sigma_1)] [f_2(x, \mu_{1/2,2}, \sigma_2)] \\
& = \frac{1}{\sqrt{2\pi\sigma_1^2}} e^{-(x - \mu_{\frac{1}{2},1})^2 8f(\mu_{\frac{1}{2},1})^2 m} \times \frac{1}{\sqrt{2\pi\sigma_2^2}} e^{-(x - \mu_{\frac{1}{2},2})^2 8f(\mu_{\frac{1}{2},2})^2 m} \\
& = \frac{1}{2\pi\sqrt{\sigma_1^2\sigma_2^2}} e^{-(x - \mu_{\frac{1}{2},1})^2 8f(\mu_{\frac{1}{2},1})^2 m + (x - \mu_{\frac{1}{2},2})^2 8f(\mu_{\frac{1}{2},2})^2 m} \quad (20)
\end{aligned}$$

This resulted to a newly fused distribution function:

$$\begin{aligned}
& f_{\text{fused}}(x, \mu_{\frac{1}{2},\text{fused}}, \sigma_{\text{fused}}) \\
& = \frac{1}{\sqrt{2\pi\sigma_{\text{fused}}^2}} e^{-\left(x\sqrt{8f(\mu_{\frac{1}{2},\text{fused}})^2 m} - \mu_{\frac{1}{2},\text{fused}}\sqrt{8f(\mu_{\frac{1}{2},\text{fused}})^2 m}\right)^2} \quad (21)
\end{aligned}$$

where

$$\begin{aligned}
\sigma_{\text{fused}}^2 & = \frac{\sigma_1^2\sigma_2^2}{\sigma_1^2 + \sigma_2^2} = \frac{(8f(\mu_{\frac{1}{2},1})^2 m)^{-1}\sigma_2^2}{\sigma_1^2 + \sigma_2^2} \\
& = \frac{1}{(8f(\mu_{\frac{1}{2},1})^2 m)} \cdot \frac{\sigma_2^2}{\sigma_1^2 + \sigma_2^2} \quad (22)
\end{aligned}$$

and

$$\begin{aligned}
\mu_{\frac{1}{2},\text{fused}} & = \frac{\mu_{\frac{1}{2},1}\sigma_2^2 + \mu_{\frac{1}{2},2}\sigma_1^2}{\sigma_1^2 + \sigma_2^2} = \mu_{\frac{1}{2},1} + \frac{\sigma_1^2(\mu_{\frac{1}{2},2} - \mu_{\frac{1}{2},1})}{\sigma_1^2 + \sigma_2^2} \\
& = \frac{\mu_{\frac{1}{2},1}}{g} + \frac{(\frac{\sigma_1}{g})^2(\mu_{\frac{1}{2},2} - \frac{\mu_{\frac{1}{2},1}}{g})}{(\frac{\sigma_1}{g})^2 + \sigma_2^2} \\
& = \mu_{\frac{1}{2},1} + \left[\frac{\frac{\sigma_1^2}{g}}{(\frac{\sigma_1}{g})^2 + \sigma_2^2}\right] [\mu_{\frac{1}{2},2} - \frac{\mu_{\frac{1}{2},1}}{g}] \quad (23)
\end{aligned}$$

Note the information from the prediction could be scaled by a parameter g . According to the definition II.4 and (12), substituting $\tilde{\mu} = \mu + \sigma - f(\mu_{\frac{1}{2}})$, $H = 1/g$ and $K = (H\sigma_1^2)/(H^2\sigma_1^2 + \sigma_2^2)$ in (23) gives,

$$\begin{aligned}
\mu_{\frac{1}{2},\text{fused}} & = \mu_1 + \frac{\sigma_1}{g} - f(\mu_{\frac{1}{2},1}) + \left[\frac{\frac{\sigma_1^2}{g}}{(\frac{\sigma_1}{g})^2 + \sigma_2^2}\right] [\mu_2 + \sigma_2 \\
& - f(\mu_{\frac{1}{2},2}) - \mu_1 - \frac{\sigma_1}{g} + f(\mu_{\frac{1}{2},1})] \\
& = \mu_1 + \sqrt{\sigma_1^2} - f(\mu_{\frac{1}{2},1}) + K(\mu_2 + \sigma_2 - f(\mu_{\frac{1}{2},1}) \\
& - H_t\mu_1 - H_t^2\sigma_1 + H_t f(\mu_{\frac{1}{2},1})) \quad (24)
\end{aligned}$$

Comparing the terms derived from (22) to (24) to the standard vectors and matrices used in the Kalman filter algorithm generated the following relationships:

- The state prediction $\mu_{1/2,1} \approx \hat{x}_{t|t-1}$,
- The measurement vector $\mu_{1/2,2} \approx z_t$,
- The state estimate generated from data fusion $\mu_{1/2,\text{fused}} \approx \hat{x}_{t|t}$,
- The *a-priori* estimate covariance matrix $\sigma_1^2 \approx P_{t|t-1}$,
- Covariance matrix of estimation error $\sigma_2^2 \approx R_t$,
- The *a-posteriori* estimate covariance matrix $\sigma_{\text{fused}}^2 \approx P_{t|t}$,
- The transformation observation matrix $H \approx H_t$, and
- The Kalman gain $K \approx K_t$.

This led to the formulation of (25) from (24), and (26) from (22) as shown below:

$$\begin{aligned}
\hat{x}_{t|t} & = \hat{x}_{t|t-1} + H_t \sqrt{P_{t|t-1}} - f(\tilde{x}_{t|t-1}) + K_t [z_t + \sqrt{R_t} \\
& - f(\tilde{z}_t) - H_t \hat{x}_{t|t-1} - H_t^2 \sqrt{P_{t|t-1}} + H_t f(\tilde{x}_{t|t-1})] \quad (25)
\end{aligned}$$

$$P_{t|t} = K_t (64f(\tilde{x}_{t|t-1})^2 f(\tilde{x}_t)^2 P_{t|t-1} R_t)^{-1} \quad (26)$$

They represented the updated measurement equations of the filtering step. To improve the initialization procedure, a smoother process was introduced. It analyzes a sequence of T observations from the previous filter measurements. Here, the time sequence was turned backwards such that $t = T, T-1, \dots, 0$. This sequence updated the smoothed *a-posteriori* estimate covariance, $P_{t|T}^S$. The subscript S denotes the smooth operator. Taking the difference between (25) and (1), and then its update with respect to the state estimate of the forward run gives:

$$x_t - \hat{x}_{t|t-1} = F_t P_{t+1|T}^S F_t^T + H \sqrt{P_{t+1|T}^S} - f(\tilde{x}_{t|t-1}) + \mathbf{E}_{\mu_{1/2}}$$

$$\begin{aligned}
& [(K_t H_t x_t + K_t \nu_t + K_t \sqrt{R_t} - K_t f(\tilde{z}_t) - K_t H_t \\
& \hat{x}_{t|t-1} - K_t H_t^2 \sqrt{P_{t+1|T}^S} + K_t H_t f(\tilde{x}_{t|t-1}) - w_t) \\
& (K_t H_t x_t + K_t \nu_t + K_t \sqrt{R_t} - K_t f(\tilde{z}_t) - K_t H_t \\
& \hat{x}_{t|t-1} - K_t H_t^2 \sqrt{P_{t+1|T}^S} + K_t H_t f(\tilde{x}_{t|t-1}) - w_t)^T] \\
P_{t|T}^S &= F_t P_{t+1|T}^S F_t^T + H_t \sqrt{P_{t+1|T}^S} - f(\tilde{x}_{t|t-1}) + \\
& [(K_t H_t f(\tilde{P}_{t+1|T}^S) - K_t H_t^2 \sqrt{P_{t+1|T}^S} + K_t \sqrt{R_t} \\
& - K_t H_t \hat{x}_{t|t-1} + K_t f(\tilde{R}_t) + w_t (K_t - 1))(K_t H_t \\
& f(\tilde{P}_{t+1|T}^S) - K_t H_t^2 \sqrt{P_{t+1|T}^S} + K_t \sqrt{R_t} - K_t \\
& f(\tilde{z}_t) - K_t H_t \hat{x}_{t|t-1} + K_t f(\tilde{R}_t) + w_t \\
& (K_t - 1))^T] \quad (27) \\
\hat{x}_{t|T} &= \hat{x}_{t|t-1} + P_{t|T}^S \quad (28)
\end{aligned}$$

where using definition II.1, $\mathbf{E}_{\mu_{1/2}}(x_t - \hat{x}_{t|t-1}) = f(\tilde{P}_{t+1|T}^B)$. R_t denotes the covariance matrix of the difference between z_t and $H_t x_t$. F_t is the state transition model applied to previous state x_{t-1} . The desired measurement update for the state estimate is $\hat{x}_{t|T}$.

Up to now, a one-dimensional example was used to derive the scalar mathematics. This could now help us to generate the residuals from the estimated temperature and voltage of the battery system.

B. Residual Generation

The residual generation of the estimated parameters depends on the following two assumptions. They are summarized as follows:

Assumption II.2: For each measurement, there exists L_0 such that for any norm bounded $x_{1,t}, x_{2,t} \in \mathbf{R}^n$, the following inequality holds:

$$\|(u_t, z_t, x_{1,t}) - (u_t, z_t, x_{2,t})\| \leq L_0 \|x_{1,t} - x_{2,t}\| \quad (29)$$

Assumption II.3: Considering the simplified form of (1), the transfer function matrix $H_t[sI - (A_t - K_t H_t)]^{-1} B_t$ is strictly positive real, where $K_t \in \mathbf{R}^{n \times r}$ is chosen such that $A_t - K_t H_t$ is stable.

Assume a given positive definite matrix $Q_t > 0 \in \mathbf{R}^{n \times n}$ at time instant t . There should exist a covariance matrix, $P_t = P_t^* > 0 \in \mathbf{R}^{n \times n}$, and a scalar covariance error R_t such that:

$$(A_t - K_t H_t)^* P_t (A_t - K_t H_t) = -Q_t \quad (30)$$

$$P_t B_t = H_t^* R_t \quad (31)$$

To detect a fault from a residual generation for each measurement, the following expression was constructed:

$$\hat{x}_t = A_t \hat{x}_t + (u_t, z_t) + \xi_{f,t}(u_t, z_t, \hat{x}_t) + K_t(z_t - \hat{z}_t) \quad (32)$$

$$\hat{z}_t = H_t \hat{x}_t \quad (33)$$

$$r_t = V(z_t - \hat{z}_t) \quad (34)$$

where the pair (A_t, H_t) is assumed. The $\xi_t \in \mathbf{R}$ is a parameter that changes unexpectedly when a fault occurs. The variable V is the residual weighting matrix. Since the pair (A_t, H_t) is assumed observable, K_t could be selected to ensure $A_t - K_t H_t$ is a stable matrix. This could be defined as:

$$e_{x,t} = x_t - \hat{x}_t, \quad e_{z,t} = z_t - \hat{z}_t \quad (35)$$

Error equations became:

$$\begin{aligned}
e_{x,t+1} &= (A_t - K_t H_t)e_{x,t} + [\xi_t(u_t, z_t, x_t) \\
&\quad - \xi_{f,t}(u_t, z_t, \hat{x}_t)], \quad (36)
\end{aligned}$$

$$e_{z,t} = H_t e_{x,t} \quad (37)$$

The convergence of the above filter was guaranteed by the following theorem II.2:

Theorem II.2: Based on Assumption II.3, the filter is asymptotically convergent when no fault occurs ($\xi_t = \xi_{f,t}$), i.e. $\lim_{t \rightarrow \infty} e_{z,t} = 0$.

Proof of Theorem II.2: This is shown in the Appendix. ■

Once the residual was found, evaluations were required to determine the threshold selection for identifying a fault.

C. Residual Evaluation

The residual evaluation was performed by a coherence function. Such approach is widely used in system identification or in determining the cause-effect relationship of a system with its applications [32, 33]. In this work, a function based on magnitude of squared coherence spectrum was employed to determine the fault status of a battery system at its outputs. Let $\hat{G}(\omega)$ and $\hat{G}_f(\omega)$ be the estimates of the frequency response of the battery system under normal fault-free and faulty operating output regimes respectively. Here ω is the frequency in *rad/sec*. The magnitude-squared coherence spectrum of the two signals could be defined as:

$$c(\hat{G}(\omega), \hat{G}_f(\omega)) = \frac{|\hat{G}(\omega)\hat{G}_f^*(\omega)|^2}{|\hat{G}(\omega)|^2|\hat{G}_f(\omega)|^2} \quad (38)$$

where $c(\hat{G}(\omega), \hat{G}_f(\omega))$ is the magnitude-squared coherence spectrum, and $\hat{G}_f^*(\omega)$ is the complex conjugate of $\hat{G}_f(\omega)$. The coherence spectrum would be less than or equal to unity due to the normalization terms in the denominator

$$c(\hat{G}(\omega), \hat{G}_f(\omega)) \leq 1 \quad (39)$$

In the presence of noise, a threshold value was estimated to give a high probability of detection and a low probability of false alarms. The test statistic $test_{stat}$ was chosen to be the median value of the coherence spectrum

$$test_{stat} = \mu_{1/2}(c(\hat{G}(\omega), \hat{G}_f(\omega))) \quad (40)$$

$$test_{stat} = \begin{cases} \leq th \quad \forall \omega \in \Omega \text{ fault} \\ > th \quad \forall \omega \in \Omega \text{ no fault} \end{cases} \quad (41)$$

where $0 \leq th \leq 1$ is a threshold value, Ω is the relevant spectral region, e.g. bandwidth. The evaluation output can be treated as a detection signal for fault isolation.

Note that in cases of incipient residual evaluation, noise is considered as an inherent component of system measurement. Therefore, it is likely that a single input-single output system is insufficient to capture the complete system dynamics due to insufficient ideal system assumptions. A CauchySchwarz inequality is then considered to guarantee a value of $c(\hat{G}(\omega), \hat{G}_f(\omega)) \leq 1$. To achieve precise threshold selection for a particular signal, only a fractional part of the output signal will be considered by the input of that frequency. This leads to the definition of the coherent output spectrum as:

$$G_0(\omega) = (c(\hat{G}(\omega), \hat{G}_f(\omega)))\hat{G}_f(\omega) \quad (42)$$

where $G_0(\omega)$ provides a spectral quantification of the output power that is uncorrelated with noise or other inputs.

D. Fault Isolation using the Recognition Model

The fault isolation was based on a recognition model, which directly relates the recognition parameters to the input and output of the battery system. The recognition model linking to the reference input r , the recognition parameter γ , and the residual error e_t is:

$$e_t = y_t - y_t^0 = \sum_{i=1}^q \psi_{t-1}^T \theta_i^{(1)} \Delta\gamma_i + \nu_t \quad (43)$$

where, $\Delta\gamma_i = \gamma - \gamma_i^0$ is the perturbation in γ ; y_t and y_t^0 are the fault-free (nominal) and faulty outputs, respectively. $\theta_i^{(1)} = \frac{\delta\theta}{\delta\gamma_i}$, and ψ is the data vector formed of the past outputs and past reference inputs. The gradient $\theta_i^{(1)}$ was estimated by performing a number of offline experiments, which consisted of perturbing the recognition parameters one at a time. The input-output data from all the perturbed parameter experiments were then used to identify the gradients $\theta_i^{(1)}$. The outcome could be represented in the form of the cross-spectral density between the faulty data and fault-free data.

E. Summary of MEDA Approach

1. *ME-based KS*: Define the properties of Median expectation operator from (3) to (14). Deriving the state and covariance matrices for filter from (25) to (26), following by a smoother from (27) to (28).
2. *Residual Generation*: Generate the residual of the estimated parameters outlined from (29) to (37).
3. *Residual Evaluation*: Evaluate the residual using coherence function from (38) to (42).
4. *Fault Isolation*: Fault isolation is calculated using the recognition model outlined in (43).

III. IMPLEMENTATION AND EVALUATION

The proposed FDI scheme was exhaustively assessed on Lithium-ion battery under different operating conditions. Two case studies were presented in this paper. Test Case I analyzed the HEV duty cycle data and Test Case II evaluated the PHEV duty cycle measurements obtained from experiments conducted at the Center of Automotive Research [15]. Experiments followed the guidelines issued by United States Department of Energy battery test manual [18, 34]. In both test cases, the characterized battery cell is a cylindrical A123 ANR26650 lithium-ion iron-phosphate cell with nominal capacity of 2.3 Ah and nominal voltage of 3.2 V. The experimental setup is composed of 800 W programmable electronic load, 1.2 kW programmable power supply, a data acquisition unit for collecting measurement signals, a thermal chamber to provide a controlled thermal environment, and a computer used for controlling the current load and supply and data storage through a Labview interface. The noise in the measurements is eliminated with the help of a low pass filter. The characterization tests and driving cycle test were conducted with a frequency of 10 Hz at 20 °C, and the current is considered to be positive at discharge and negative at charge. In this paper, FDI was tested under offline environment because of two main reasons. One was the fault injection typically resulted in a detection by BMS. This detection could result

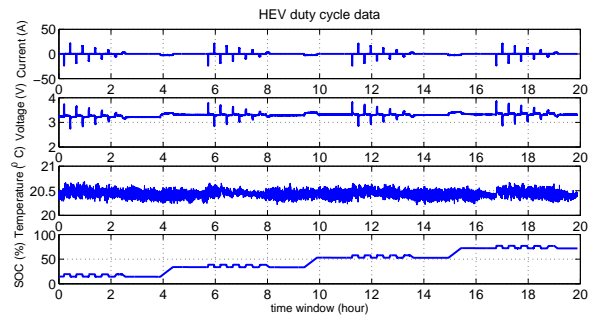


Fig. 3. Li-ion battery cell measurements with HEV duty cycle

in system shut-off or a compensation of the fault. Alternatively, if the BMS was unavailable, it could not detect the fault. In this case, the injected fault may result in potential damage to battery. Therefore, while the scheme was designed to operate in real-time, the off-line approach was chosen as the whole set of considered faults were covered in a consistent way.

In this paper, frozen and biased sensor faults were considered for voltage and temperature sensor measurements, respectively. They were applied at random timings in both cases. The following performance metrics were formulated to evaluate the effectiveness of the proposed MEDA based health monitoring scheme:

- DT: Time from the fault occurrence to first sensitive detection of fault.
- MDR: The ratio of test runs for which the fault occurrence was not detected.
- FDR: The ratio of test runs for which the fault occurrence was detected under no-fault condition
- IT: Time from fault occurrence to first correct isolation of fault.
- MIR: The ratio of test runs for which the correct fault isolation was not obtained.

A. Test Case I: Li-ion Battery Cell under HEV Duty Cycle

The HEV charge-sustaining operations were performed at each 10 % SoC intervals. The hybrid pulse test data was composed of constant charge and discharge current pulses of magnitudes ranging from 1A to 10A to identify the battery model parameters. Each discharge pulse was followed by a corresponding charge pulse such that the overall profile was a charge neutral at a given SoC. This discharge and charge current pulses could improve the applicability of model under a more broad current ranges [15]. After several charge neutral around a given SoC, a 1A current was conducted to set SoC for the next set of current demands followed by a half-hour rest period to ensure the system reaches electrochemical and thermal equilibrium. The entire test was based on the charging and discharging operations. The sampled current, corresponding voltage and temperature profiles, and SoC trajectory during the charging operation are shown in Fig. 3.

The proposed FDI scheme was implemented to first estimate the voltage and temperature dynamics from the real-time current measurements of the Li-ion battery cell under HEV duty cycle as shown in Fig. 3. Referring to Fig. 4, the proposed median-based Kalman filter and its derived smoother were used

TABLE I
PERFORMANCE EVALUATION OF FAULTS IN HEV¹

Metric	DT _{EKF}	DT _{MKF}	DT _{MKS}	MDR _{EKF}	MDR _{MKF}	MDR _{MKS}	FDR _{EKF}	FDR _{MKF}	FDR _{MKS}	IT	MIR
ΔV_{HEV}	28.403	19.036	19.247	0	0	0	0.046	0.069	0.024	19.330	0.304
ΔT_{HEV}	24.536	16.229	20.132	0	0	0	0.045	0.027	0.022	10.527	0.114

¹In this table, ΔV and ΔT are the voltage and temperature faults respectively. DT is the detection time, MDR is the missed detection rate, FDR is the false detection rate, IT is the isolation time and MIR is the missed isolation rate. Subscript EKF, MKF and MKS are the acronyms of extended Kalman filter, median-based Kalman filter and median-based Kalman smoother respectively.

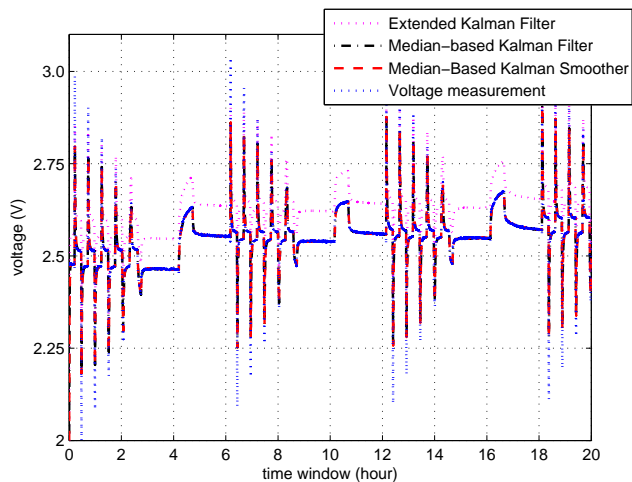


Fig. 4. Comparison of battery cell voltage estimates for HEV duty cycle

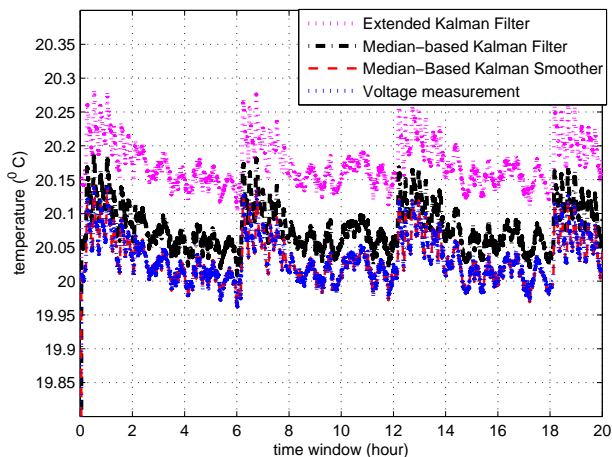


Fig. 5. Comparison of battery cell temperature estimates for HEV duty cycle

to estimate the respective output profile of the voltage. In addition, comparisons with the mainstream Extended Kalman filter of [16, 17] were made. The proposed filter and its smoothed version were observed to capture the system dynamics more clearly than the regular extended Kalman filter. Furthermore, a comparison of MSE between the main stream EKF [16, 17] and the proposed filter is shown in Fig. 6. Because of the initialization procedure, the EKF started with a slow time tracking response, causing EKF to have a higher MSE value in the initial time windows. In contrast, the median-based Kalman filter and its smoother were fast enough to capture the dynamics well from the start. Therefore, the proposed method gave more accurate results than EKF as it was able to estimate the deviations of outliers with precision. This was due to its estimating nature using the calculated median of the sample size.

The estimated temperature output profile of battery cell in

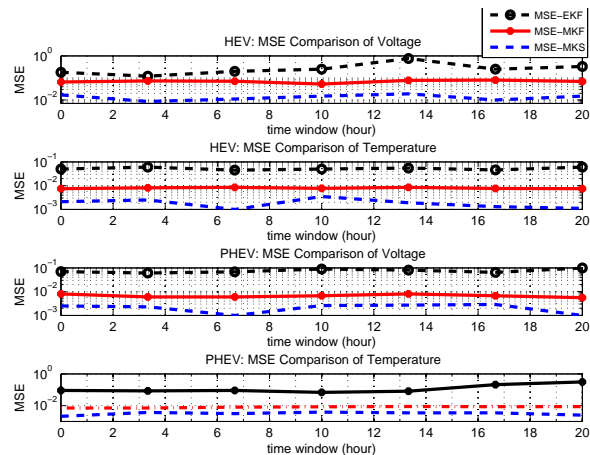


Fig. 6. MSE performance of estimated battery parameters

HEV duty cycle is illustrated in Fig. 5. Since the temperature dynamics were not varying significantly, all estimation schemes performed reasonably well. The dynamics of temperature were being captured well by the regular Extended Kalman filter. Furthermore, a comparison of MSE is shown in Fig. 6. All schemes performed reasonably well. However, EKF was not able to estimate the fault thoroughly. This may be due to its linear nature.

Once the estimation accuracy has been achieved, the residuals were generated. Random fault was then introduced into each output profile. This occurred at 13.0-14.0 hours and 9.8-10.9 hours for voltage and temperature profiles, respectively. Referring to Fig. 7, both faults were detected using the threshold selection by coherence function. The threshold selected for voltage and temperature residuals were ± 1 and ± 10 , respectively. As observed in Fig. 7(a), some wiggles in the residual correspond to the dynamics of real-time data. However, they could also be mistaken as faults if inappropriate threshold was selected. In this case, the threshold selection algorithm was good enough to detect the faults while avoiding the false alarms. Subsequently, accurate detection signal was generated for fault isolation. Referring to Fig. 8, fault isolation was made by cross spectral density analysis. It was observed that the fault was isolated accurately in both cases. Finally the performance evaluation of BMS was evaluated.

Table I summarizes the DT, MDR, FDR, IT and MIR for all considered faults. Note the DT and IT are given in seconds. It could be seen that both voltage and temperature sensor faults were detected within reasonable time. The MKF and MKS were significantly faster when comparing to the slower battery cell dynamics. They were also accurate to report any missed detections. In addition, MKS offered a more accurate estimation of voltage and temperature profiles while having a

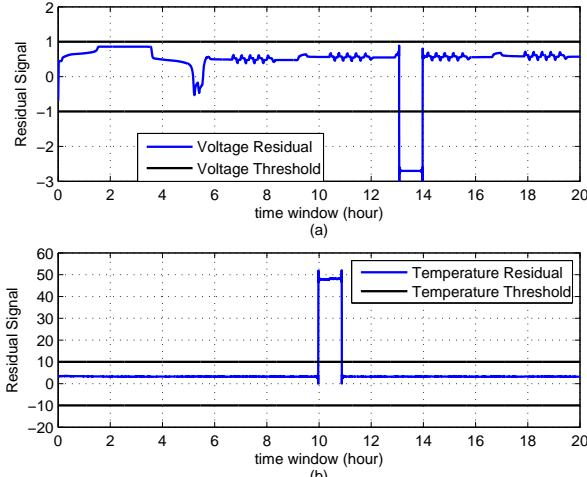


Fig. 7. a) Battery cell voltage sensor residual in HEV duty cycle, and b) Battery cell temperature sensor residual in HEV duty cycle

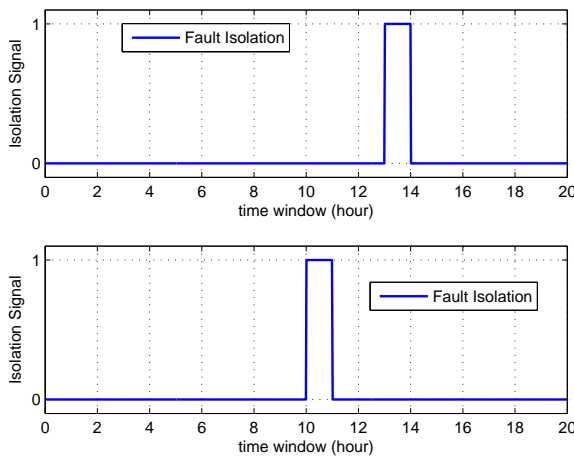


Fig. 8. a) Battery cell voltage sensor fault detection in HEV duty cycle, and b) Battery cell temperature sensor fault detection in HEV duty cycle

slightly longer time than MKF. Although the isolation ratio was quiet low for both proposed methods, there were some missed isolations. Overall, the proposed MKS took less time than the standard EKF. Moreover, the FDR of MKS was comparatively smaller than EKF.

B. Test Case II: Li-ion Battery Cell under PHEV Duty Cycle

The transient battery power test cycle was a variant of the standard DST cycle, which was used to simulate the actual driving cycles of electric vehicles. The profile was extracted from the United States Department of Energy battery test manual for PHEVs [18,34]. The sampled current profile, temperature variations and corresponding SoC trajectory are shown in Fig. 9. Referring to Fig. 10, the estimation comparison of different methods were made tracking the reference signal of voltage sensor output. The corresponding MSE between the main stream EKF and the proposed filter is shown in Fig. 6. All the schemes performed reasonably well. However, EKF was not able to estimate the temperature measurement thoroughly. This could be due to its linear nature. Meanwhile, the estimated temperature sensor output are shown in Fig. 11. The regular extended Kalman filter demonstrated decent estimation of the temperature variations.

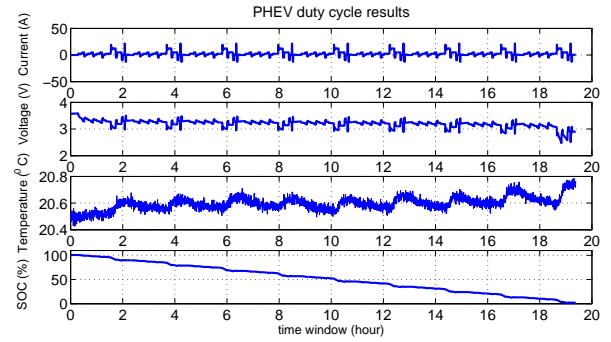


Fig. 9. Li-ion battery cell measurements for PHEV duty cycle

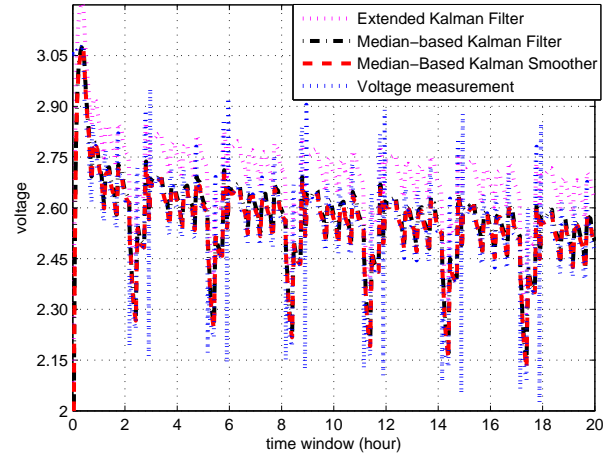


Fig. 10. Comparison of battery cell voltage estimates for PHEV duty cycle

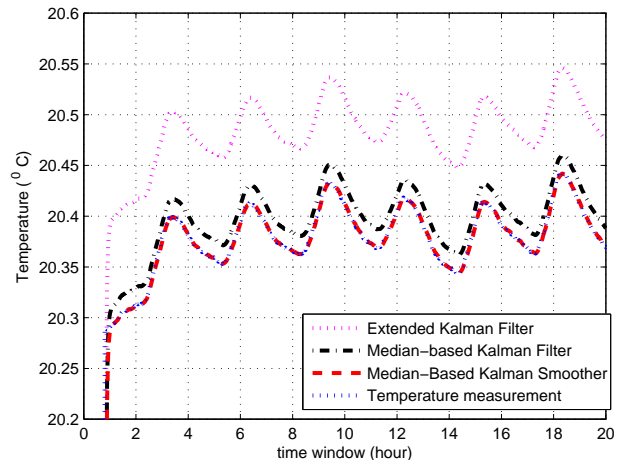


Fig. 11. Comparison of battery cell temperature estimates for PHEV duty cycle

After the state estimation, random faults were introduced in the voltage and temperature outputs at 8.1-9.0 hours and 14.3-16.0 hours, respectively. The residual fault detection using the coherence function-based threshold is made. This could be observed in Fig. 12. The threshold selected for voltage and temperature residuals were ± 1.5 and ± 1 , respectively. Fault isolation of PHEV could be seen for voltage and temperature using Fig. 13. Referring to Table II, the performance evaluation of FDI scheme was made for PHEV duty cycles. Similar to HEV test case, PHEV performed equally well to detect and isolate faults.

TABLE II
PERFORMANCE EVALUATION OF FAULTS IN PHEV

Metric	DT _{EKF}	DT _{MKF}	DT _{MKS}	MDR _{EKF}	MDR _{MKF}	MDR _{MKS}	FDR _{EKF}	FDR _{MKF}	FDR _{MKS}	IT	MIR
ΔV_{PHEV}	25.793	16.672	16.921	0	0	0	0.030	0.059	0.019	18.319	0.296
ΔT_{PHEV}	20.729	16.619	16.275	0	0	0	0.040	0.025	0.021	12.168	0.256

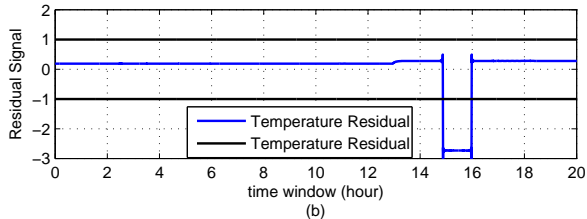
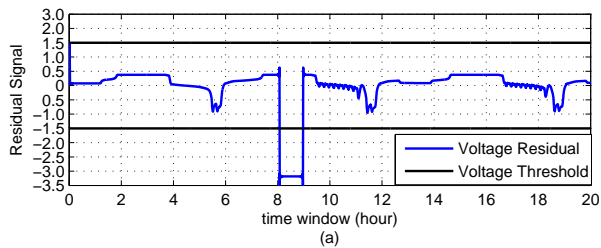


Fig. 12. a) Battery cell voltage sensor residual in PHEV duty cycle, and b) Battery cell temperature sensor residual in PHEV duty cycle

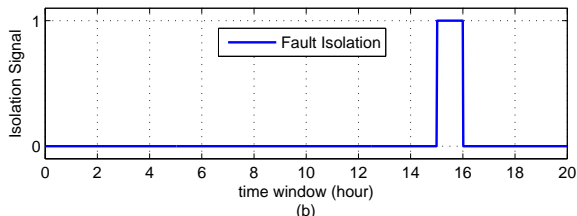
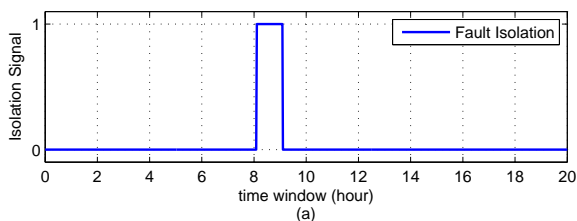


Fig. 13. a) Battery cell voltage sensor fault detection in PHEV duty cycle, and b) Battery cell temperature sensor fault detection in PHEV duty cycle

IV. CONCLUSIONS AND FUTURE RESEARCH

In this paper, the proposed MEDA based health monitoring scheme was demonstrated to estimate the output states of HEV and PHEV duty cycles. The proposed scheme was able to estimate the outliers and abrupt changes accurately. Furthermore, the detection of the injected faults were effective to report any likely false alarms. The fault diagnosis based on the proposed algorithm was able to give better results than its predecessors when random faults were generated.

In the future, studies to quantitatively verify the effectiveness and robustness of the proposed method to false measurements would be conducted. Moreover, its implementation to quantify the boundaries of the proposed method in real-time simulation would be verified. To achieve this, practical implementation of estimation and diagnostics schemes are only significant when they are part of the control strategy. Since, the diagnos-

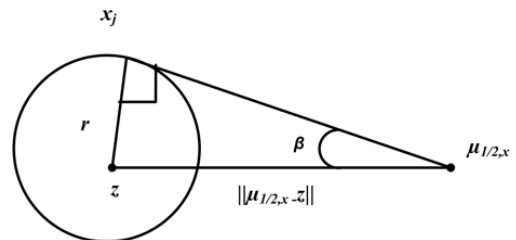


Fig. 14. Median Convergence Diagram

tic decisions may not be required for time-sensitive controller actions, an offline implementation would give more credible results. The proposed scheme could also be incorporated as a tool for on-board diagnostics (OBD), where it could give accurate diagnostic information about various vehicle subsystems. Due to its better convergence rate and estimation capability than its variants, it would allow to identify and detect malfunctions accurately and in lesser time.

ACKNOWLEDGMENT

This research was conducted on the data collected during the battery experiments done at Center for Automotive Research (CAR) at the Ohio State University (OSU). The authors would like to thank Professor Giorgio Rizzoni, the Director, CAR, OSU for his suggestions during the development of the work presented in this paper.

APPENDIX

A. Proof of (7)

Following [31], let $x_1, x_2, \dots, x_N \in H$, and let $\mu_{1/2,x}$ be their median. Assumed that $z \in H$, r was the radius such that $\|\mu_{1/2} - z\| > \beta r$ and $r > 0$ as shown in Fig. 14. There should exist a subset $J \subseteq (1, \dots, N)$ such that for all $j \in J$, $\|x_j - z\| > r$. Considering the directional derivative at the point $\mu_{1/2}$ in the direction $z - \mu_{1/2}$.

$$\nabla f(\mu_{1/2}, z - \mu_{1/2}) = \lim_{t \rightarrow 0} \frac{f(\mu_{1/2} + t(z - \mu_{1/2})) - f(\mu_{1/2})}{t} \quad (44)$$

Since $\mu_{1/2}$ minimizes the function f , this indicated that $\nabla f(\mu_{1/2}, z - \mu_{1/2}) \geq 0$. From (44), this also gave:

$$\frac{\nabla f(\mu_{1/2}, z - \mu_{1/2})}{\|z - \mu_{1/2}\|} = -\sum_{x_j \neq \mu_{1/2}} \frac{x_j - \mu_{1/2}, z - \mu_{1/2}}{\|x_j - \mu_{1/2}\| \|z - \mu_{1/2}\|} + \sum_{j=1}^N I(x_j = \mu_{1/2}) \quad (45)$$

Based on (45) that $\sum_{j=1}^N \frac{x_j - \mu_{1/2}}{\|x_j - \mu_{1/2}\|} = 0$. This helped us to show the convergence of (6) and (7).

B. Proof of Properties of Theorem II.1

Proof of Property 1:

$$\begin{aligned}
& \arg \min_{s \in H} \sum_{i=1}^N \|x_i - s\| = \mathbf{E}_{\mu_{1/2}}(X) \\
& \arg \min_{s \in H} \sum_{i=1}^N \|cx_i - s\| = \arg \min_{\frac{\tilde{s}}{c}} \sum_{i=1}^N \|cx_i - \frac{\tilde{s}}{c}\| \\
& = \min_{\tilde{s} \in cH} \sum_{i=1}^N \|cx_i - \tilde{s}\|, cH : \{ch : h \in H\} \\
& \quad \sum_{i=1}^N \|cx_i - c\mathbf{E}_{\mu_{1/2}}(x)\| = |c| \sum_{i=1}^N \|x_i - \mathbf{E}_{\mu_{1/2}}(x)\| \\
& = |c| \arg \min_{s \in H} \sum_{i=1}^N \|x_i - s\| = \arg \min_{s \in H} \sum_{i=1}^N \|cx_i - cs\| \\
& = \arg \min_{\frac{\tilde{s}}{c} \in H} \sum_{i=1}^N \|cx_i - \tilde{s}\|, \text{ where } s = \frac{\tilde{s}}{c} \\
& = \min_{\tilde{s} \in cH} \sum_{i=1}^N \|cx_i - \tilde{s}\| = \sum_{i=1}^N \|cx_i - \mathbf{E}_{\mu_{1/2}}(x)\| \\
& = \min_{\tilde{s} \in H} \sum_{i=1}^N \|cx_i - \tilde{s}\| \tag{46}
\end{aligned}$$

where $cH = H$ since H is a linear operator. ■

Proof of Property 2:

$$\begin{aligned}
& = \arg \min_{s \in H} \sum_{i=1}^N \|ax_i + by_i - s\| \\
& \leq \sum_{i=1}^N \|ax_i + by_i + a\mathbf{E}_{\mu_{1/2}}(x) + b\mathbf{E}_{\mu_{1/2}}(y)\| \\
& \leq \sum_{i=1}^N (\|ax_i + a\mathbf{E}_{\mu_{1/2}}(x)\| + \|by_i + b\mathbf{E}_{\mu_{1/2}}(y)\|) \\
& = \sum_{i=1}^N \|ax_i + a\mathbf{E}_{\mu_{1/2}}(x)\| + \sum_{i=1}^N \|by_i + b\mathbf{E}_{\mu_{1/2}}(y)\| \\
& = \min_{s \in H} \sum_{i=1}^N \|ax_i - s\| + \min_{s \in H} \sum_{i=1}^N \|by_i - s\| \\
& \leq \min_{s \in H} \sum_{i=1}^N (\|ax_i - s\| + \|by_i - s\|) \tag{47}
\end{aligned}$$

Proof of Property 3: It follows the proof of Property 2. ■

Property 4: If X was an independent variable, then for the higher moments of X , i.e. $\mathbf{E}_{\mu_{1/2}}[X^2]$,

$$\begin{aligned}
\mathbf{E}_{\mu_{1/2}}[X^2] & = \mathbf{E}_{\mu_{1/2}}[(X - \mathbf{E}_{\mu_{1/2}}[X])^2] \\
& = \arg \min_{\theta_1} \{ \|X - \arg \min_{\theta_2} \{ \|X - \theta_2\| \} \|^2 - \theta_1 \} \\
& = \arg \min_{\theta_1} \{ \|X^2 - 2X(\arg \min_{\theta_2} \|X - \theta_2\|) \\
& \quad + (\arg \min_{\theta_2} \|X - \theta_2\|)^2 - \theta_1 \} \tag{48}
\end{aligned}$$

where θ_1 and θ_2 represents the expectation $\mathbf{E}_{\mu_{1/2,1}}$ and $\mathbf{E}_{\mu_{1/2,2}}$ respectively.

C. Proof of theorem II.2:

Consider the following Lyapunov function,

$$V(e_t) = e_{x,t}^* P_t e_{x,t} \tag{49}$$

where P_t was defined as the solution of (30), Q_t was chosen such that $\rho_1 = \lambda_{\min}(Q_t) - 2\|H_t\| \cdot |R_t| \xi_{f,t} L_0 > 0$. Along the trajectory of the fault-free system, the corresponding Lyapunov difference along the trajectory e_t could be expressed as:

$$\begin{aligned}
\Delta V & = \mathbf{E}\{V(e_{t+1}|e_t, P_t)\} - V(e_t) \\
& = \mathbf{E}\{e_{t+1}^* P_t e_{t+1}\} - e_t^* P_t e_t \\
& = (A_{e,t} e_{x,t} + B_{L_0,t} u_{e,t})^* P_t (A_{e,t} e_{x,t} + B_{L_0,t} u_{e,t}) \\
& \quad - e_{x,t}^* P_t e_{x,t} \\
& = e_t^* [(P_t (A_t - K_t H_t) + (A_t - K_t H_t)^* P_t)
\end{aligned}$$

$$+ P_t B_t \xi_{f,t} [(u_t, z_t, x_t) - (u_t, z_t, \hat{x}_t)]] e_t \tag{50}$$

From Assumption II.2 and system described by (30), one could further claim:

$$\begin{aligned}
\Delta V & \leq -e_{x,t}^T Q_t e_{x,t} + 2\|e_{z,t}\| \cdot |R_t| \xi_{f,t} L_0 \|e_{x,t}\| \\
& \leq -\rho_1 \|e_{x,t}\|^2 < 0 \tag{51}
\end{aligned}$$

Thus, $\lim_{t \rightarrow \infty} e_{x,t} = 0$ and $\lim_{t \rightarrow \infty} e_{z,t} = 0$. This completed the proof.

REFERENCES

- [1] H. Budde-Meiwes, J. Drillkens, B. Lunz, J. Muennix, S. Rothgang, J. Kowal, and D. U. Sauer, "A review of current automotive battery technology and future prospects," *Jour. Auto. Engg.*, vol. 227, no. 5, pp. 761–776, 2013.
- [2] A. Burke and M. Miller, "Performance characteristics of lithium-ion batteries of various chemistries for plug-in hybrid vehicles," *EVS24 Intl. Battery, Hybrid and Fuel Cell Elec. Vehicle Symp.*, Stavanger, Norway, pp. 1–13, May 2009.
- [3] A. Dinger, R. Martin, X. Mosquet, M. Rabl, D. Rizoulis, M. Russo, and G. Sticher, "Batteries for electric cars: Challenges, opportunities, and the outlook to 2020," *tech. rep., The Boston Consulting Group*, 2010.
- [4] M. Lowe, S. Tokuko, T. Trigg, and G. Gereffi, "Lithium-ion batteries for electric vehicles," *tech. rep., Center of Glob., Governance & Competitiveness*, Duke Uni., Oct. 5, 2010.
- [5] L. G. Lu, X. B. Han, J. Q. Li, J. F. Hua, and M. G. Ouyang, "A review on the key issues for lithium-ion battery management in electric vehicles," *J. Power Sour.*, vol. 226, pp. 272–288, Mar. 2013.
- [6] P. Arora, R. E. White, and M. Doyle, "Capacity fade mechanisms and side reactions in lithium-ion batteries," *J. Electrochem. Soc.*, vol. 145, no. 10, pp. 3647–3667, Apr. 1998.
- [7] L. Lu, X. Han, J. Li, J. Hua, and M. Ouyang, "A review on the key issues for lithium-ion battery management in electric vehicles," *J. Power Sour.*, vol. 226, pp. 272–288, 2013.
- [8] K. Zaghbi, M. Dontigny, "Safe and fast-charging Li-ion battery with long shelf life for power applications," *J. Power Sour.* vol. 196, pp. 3949–3954, 2011.
- [9] X. Han, M. Ouyang, L. Lu, J. Li, Y. Zheng, and Z. Li, "A comparative study of commercial lithium-ion battery cycle life in electrical vehicle: Aging mechanism identification," *J. Power Sour.*, vol. 251, pp. 38–54, 2013.
- [10] D. P. Abraham, E. P. Roth, R. Kosteki, K. McCarthy, S. MacLaren, S., and D. H. Doughty, "Diagnostic examination of thermally abused high-power lithium-ion cells," *J. Power Sour.*, vol. 161, no. 1, pp. 648–657, Oct. 2006.
- [11] Q. S. Wang, P. Ping, X. J. Zhao, G. Q. Chu, J. H. Sun, and C. H. Chen, "Thermal runaway caused fire and explosion of lithium-ion battery," *J. Power Sour.*, vol. 208, pp. 210–224, Jun. 2012.
- [12] C. Mikolajczak, M. Kahn, K. White, K., and R. T. Long, R.T. "Lithium-ion batteries hazard and use assessment," *Fin. Rpr. Fire Protect. Res. Foun.*, Jul. 2011.
- [13] H. D. Daniel, and A. P. Ahmad, "Vehicle battery safety roadmap guidance," *Battery Safety Consulting (subcontractor), NREL Report No.SR-5400-54404*, Oct. 2012.
- [14] Z. Liu, Q. Ahmed, G. Rizzoni, and H. He, "Fault detection and isolation for lithium-ion battery system using structural analysis and sequential residual generation," *7th ASME Annual Dynamic Sys. and Ctrl.*, TX, US, 2014.
- [15] Y. Hu, S. Yurkovich, Y. Guezennec, and B. J. Yurkovich, "Electro-thermal battery model identification for automotive applications," *J. Power Sour.*, vol. 196, no. 1, pp. 449–457, Jan. 2011.
- [16] A. Singh, A. Izadian, and S. Anwar, "Adaptive nonlinear model-based fault diagnosis of Li-ion Batteries," *IEEE Trans. Indus. Elect.*, Article in Press, DOI: 10.1109/TIE.2014.2336599, Jul. 2014.
- [17] H. He, R. Xiong, X. Zhang, F. Sun, and J. Fan, "State-of-Charge estimation of the lithium-ion battery using an adaptive extended Kalman filter based on an improved Thevenin model," *IEEE Trans. Vehi. Tech.*, vol. 60, no. 4, pp. 1461–1469, May 2011.
- [18] J. Marcicki, M. Canova, M., A. T. Conlisk, and G. Rizzoni, "Design and parametrization analysis of a reduced-order electrochemical model of graphite/LiFePO₄ cells for SOC/SOH estimation," *Jour. Power Sour.*, vol. 237, pp. 310–324, Sep. 2013.
- [19] S. F. Schmidt, "The Kalman filter: Its recognition and development for aerospace applications," *AIAA J. Guid. Contr.*, vol. 4, pp. 4–7, 1981.

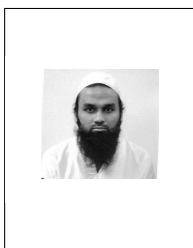
- [20] M. S. Grewal, V. Henderson, V., and R. Miyasako, R., "Application of Kalman filtering to the calibration and alignment of inertial navigation systems," *IEEE Trans. Automat. Contr.*, vol. 36, no. 1, pp. 4–14, Jan. 1991.
- [21] Grewal, M. S., Weill, L. R., and Andrews, A. P., "Global positioning systems, inertial navigation, and integration," *2nd ed. Hoboken, NJ: Wiley*, 2007.
- [22] E. Kaplan, E., and C. Hegarty, "Understanding GPS: Principles and applications, Second Edition," *Norwell, MA, USA: Artech House*, 2005.
- [23] H. Hijazi, and L. Ros, "Joint data QR-detection and Kalman estimation for OFDM time-varying Rayleigh channel complex gains," *IEEE Trans. Commun.*, vol. 58, no. 1, pp. 170–178, Jan. 2010.
- [24] C. Komninakis, C. Fragouli, A. Sayed, and R. Wesel, "Multi-input multi-output fading channel tracking and equalization using Kalman estimation," *IEEE Trans. Sig. Process.*, vol. 50, no. 5, pp. 1065–1076, May 2002.
- [25] H. M. Khalid and J. C.-H. Peng, "Improved recursive electromechanical oscillations monitoring scheme: A novel distributed approach," *IEEE Trans. Pow. Syst.*, vol. 30, no. 2, pp. 680–688, Mar. 2015.
- [26] B. S. Everitt, "The Cambridge dictionary of statistics," *Cambridge University Press*, Cambridge.
- [27] H. Cardot, P. Cenac, P., and M. Chaouch, "Stochastic approximation to the multivariate and the functional median," *Compstat 2010*, Physica Verlag, Springer, pp. 421–428, 2010.
- [28] C. Mallows, "Another comment on O'Kinneide," *The American Statistician*, vol. 45, no. 3, pp. 257, Aug. 1991.
- [29] S. Stigler, "Studies in the history of probability and statistics XXXII: Laplace, Fisher and the discovery of the concept of sufficiency," *Biometrika*, vol. 60, no. 3, pp. 439–445, Dec. 1973.
- [30] R. Faragher, "Understanding the basis of the Kalman filter via a simple and intuitive derivation," *IEEE Sig. Process. Mag.*, pp. 128–132, Aug. 2012.
- [31] M. Stanislav, "Geometric median and robust estimation in banach spaces," pp. 1–28, *arXiv: math.ST/1308.1334*.
- [32] T. Yanagisawa, H. Takayama, "Coherence coefficient measuring system and its application to some acoustic measurements," *Applied Acoustics*, vol. 16, no. 2, pp. 105–119, Mar. 1983.
- [33] C. Zheng, H. Yang, and X. Li, "On generalized auto-spectral coherence function and its applications to signal detection," *IEEE Sig. Process. let.*, vol. 21, no. 5, pp. 559–563, May 2014.
- [34] "Battery test manual for Plug-In hybrid electric vehicles," *U.S. Dept. Ener. Vehicle Tech. Program*, Revision 0, Mar. 2008.



Jimmy C. -H. Peng (S'05-M'12) received the B.E. (Hons.) and Ph.D. degrees from the University of Auckland, Auckland, New Zealand, in 2008 and 2012, respectively. In 2012, he joined the Department of Electrical Engineering and Computer Science at Masdar Institute of Science and Technology, Abu Dhabi, United Arab Emirates, as an Assistant Professor of Electrical Power Engineering. He was a Visiting Scientist with the Research Laboratory of Electronics (RLE) and a Visiting Assistant Professor with the MIT-MI Cooperative Program at Massachusetts Institute of Technology (MIT), in 2013 and 2014, respectively. His research interests are power system stability, synchrophasor measurements, real-time system identification, and high performance computing.



Haris M. Khalid (M'13) received his M.S and Ph.D. degrees from King Fahd University of Petroleum and Minerals (KFUPM), Dhahran, Kingdom of Saudi Arabia, in 2009 and 2012, respectively. He has worked as a research fellow at Distributed Control Research Group at KFUPM. Since 2013, he has been working as a Postdoctoral Researcher with Department of Electrical Engineering and Computer Science at Masdar Institute of Science and Technology (MI) collaborated with MI-MIT Cooperative Program. His research interests are power systems, signal processing, fault diagnostics, filtering, estimation, performance monitoring and battery management systems.



Qadeer Ahmed (M'11) received the B.S. degree in mechatronics and control engineering from the University of Engineering and Technology, Lahore, Pakistan, in 2007 and the M.S. and PhD degree in control systems from Mohammad Ali Jinnah University, Islamabad, Pakistan, in 2009 and 2011. He is currently Senior Research Associate at The Ohio State University, Center for Automotive Research. He is working on next generation of energy efficient vehicle power-trains. He has authored more than 33 international publications. His research interests include modeling, estimation, control and diagnostics of automotive systems.